

Automated counting of cerebral penetrating vessels using optical coherence tomography images of a mouse brain in vivo

Woo June Choi¹ | Yuandong Li² | Ruikang K. Wang² | Jun Ki Kim^{3,4}

¹School of Electrical and Electronics Engineering, Chung-Ang University, Seoul, Republic of Korea

²Department of Bioengineering, University of Washington, Seattle, Washington, USA

³Department of Convergence Medicine, University of Ulsan College of Medicine, Seoul, Republic of Korea

⁴Asan Institute for Life Science, Asan Medical Center, Seoul, Republic of Korea

Correspondence

Jun Ki Kim, Asan Institute for Life Science, Asan Medical Center, 88, Olympic-ro 43-gil, Songpa-gu, Seoul 05505, Republic of Korea. Email: kim@amc.seoul.kr

Funding information

Basic Science Research Program, Grant/Award Numbers: 2020R1F1A107403311, 2020R1F1A1072912, 2019R1A2C2084122; Engineering Research Center (ERC), Grant/Award Number: 2020R1A5A1018052; Medical Research Center (MRC), Grant/Award Number: 2018R1A5A2020732; Industry and Energy under the Industrial Technology Innovation Program, Grant/Award Number: 20000843; Ministry of Health and Welfare, the Korea Health Industry Development Institute (KHIDI), Grant/Award Number: HI18C2391

Abstract

Rationale and objectives: Penetrating blood vessels emanating from cortical surface vasculature and lying deep in the cortex are essential vascular conduits for the shuttling of blood from superficial pial vessels to the capillary beds in parenchyma for the nourishment of neuronal brain tissues. Locating and counting the penetrating vessels is beneficial for the quantification of a course of ischemia in blood occlusive events such as stroke. This paper seeks to demonstrate and validate a method for automated penetrating vessel counting that uses optical coherence tomography (OCT).

Materials and methods: This paper proposes an OCT method that effectively identifies and grades the cortical penetrating vessels in perfusion. The key to the proposed method is the harnessing of vascular features found in the penetrating vessels, which are distinctive from those of other vessels. In particular, with an increase in the light attenuation and flow turbulence, the contrast in the mean projection of the OCT datacube decreases, whereas that in the maximum projection of the Doppler frequency variance datacube increases. By multiplying the inversion of the former with the latter, its binary thresholding is sufficient to highlight the penetrating vessels and allows for their counting over the projection image.

Results: A computational method that leverages the decrease in mean OCT projection intensity and the increase in Doppler frequency variance at the penetrating vessel is developed. It successfully identifies and counts penetrating vessels with a high accuracy of over 87%. The penetrating vessel density is observed to be significantly reduced in the mouse model of focal ischemic stroke.

Conclusion: The OCT analysis is effective for counting penetrating blood vessels in mice brains and may be applied to the rapid diagnosis and treatment of stroke in stroke models of small animals.

KEYWORDS

14.11 Segmentation, 14.3 Optical computed tomography, 17.1 Image processing, 17.7 Classification methods, 17.8 Image segmentation, automated vessel counting, cerebral penetrating vessels, Doppler frequency variance, ischemic stroke, light attenuation, optical coherence tomography

1 | INTRODUCTION

In the cerebral cortex, penetrating arterioles and venules are deep-lying, narrow-diameter blood vessels that descend and ascend, respectively, into the brain tissues to shuttle blood between superficial pial vessels

and subsurface microvascular beds, thereby feeding the surrounding neuronal tissues.¹ Sustainable blood delivery via these bridging vessels to the deep capillaries is critical for powering neural activities and maintaining brain function. Disruptive blood flow in the penetrating vessels is directly associated with blood

occlusive events, such as strokes.^{1,2} During a stroke, the superficial cortex is slightly robust to blood occlusion owing to its highly collateralized surface networks with extensive anastomoses, whereas the penetrating vessels, with loosely interconnected vasculature, lack anastomoses.^{2–5} Therefore, clots in individual penetrating vessels can induce a decrease in the blood supply to the deep vascular plexus, instantly inducing highly localized ischemia, followed by cortical microinfarcts, which progressively extend throughout the depth of the cortex with 0.1–1-mm sizes.^{2,6,7} Consequently, local cellular metabolism is inhibited, leading to cognitive decline.⁶

In addition, causal associations between these infarcts and neurodegenerative diseases such as Alzheimer's disease (AD) have been reported, revealing that the infarcts may be involved in the disease-induced dysfunction of cerebrovascular networks, including the penetrating vasculatures.^{8,9} For example, a rat AD model exhibits excessive amyloid- β peptide deposited on the penetrating arterioles, and the amyloid aggregates impair the vascular function of the penetrating vessels, which may lead to ischemia episodes.⁸ This functional impairment of penetrating vessels is particularly relevant owing to its critical role in routing blood to the cortical mantle. Therefore, quantifying penetrating vessel function is essential for the monitoring of ischemia and to preempt the formation of watershed cortical microinfarcts which exacerbate cognitive impairment.

A straightforward method for analyzing vessel population involves counting the number of vessels and has been employed in studies on small animals to assess vascular growth in cortical development and vascular dysfunction models of cerebral ischemia.^{5,6,10} In previous studies, the penetrating vessels were generally counted by using fluorescence angiograms of murine neocortex postmortem or *in vivo*, where vessels were identified as small circular or elliptical spots at the end of edges of the pial network, and en passant when imaging below the pial surface. In particular, such spots were counted manually. However, the localization of the penetrating vessels was dependent on the expertise and experience of the examiners. Furthermore, manual grading can be labor-intensive, and the total counts may be subject to examiner bias with respect to the large density of penetrating vessels (e.g., approximately 25 penetrating vessels are contained in a cubic millimeter of rat cortex⁶). Hence, this is not a desirable method for the accurate and rapid detection of the diving vessel population. Moreover, in previous studies, multiphoton laser scanning fluorescence microscopy was conducted to generate the cortical angiograms, thus requiring the perfusion of exogenous fluorophores for fluorescence imaging. In addition, owing to the limited field of view in the imaging (typically several hundreds of squared micrometers), image stitching is required to obtain

sufficient statistical power in the assessment, thus adding to the labor intensiveness of the method.⁵

Optical coherence tomography (OCT) and its variants have been confirmed as feasible for the counting of penetrating vessels in small animal brains.^{3,11,12} OCT is an interferometric optical imaging tool that can provide a three-dimensional (3D) tomographic image of millimeter-scale tissue volumes at micrometer-scale resolution without the use of contrast agents.^{13,14} With the development of scan protocols for OCT data acquisition, there have been functional OCT variants for blood flow imaging that commonly detect dynamic scattering signals induced by blood cells passing through the patent vessel lumen in the tissue.^{15,16} Among the OCT variants, OCT angiography (OCTA) visualizes angio-architectures in perfusion that can be obtained from time-course changes in the amplitude, phase, and complex function (phase–amplitude) of the OCT signals repeatedly scanned at the same location.^{15,17–19} Doppler OCT (DOCT) highlights the vasculatures with axial velocities of the blood flow that are parallel to the OCT probing beam, where the blood flow velocities can be derived from the Doppler frequency–induced phase difference (phase shift) between successive beam scans.^{16,17,20} In particular, given that the amplitude of the DOCT signal is completely dependent on the directionality of blood flow,¹⁶ it is commonly used for displaying the penetrating blood vessels perpendicular to the brain surface (that give rise to the maximum Doppler signal). Accordingly, in recent studies, DOCT was conducted to examine the penetrating vessels of small animal brains. However, the vessel location and counting were human-guided and manual.^{3,11}

More recently, an OCT data–based solution for the automated detection and quantification of the penetrating vessels in mice was proposed by Wei et al.¹² The method adopted a combination of conventional eigen-decomposition frequency analysis and principal component analysis (PCA) to predict spectral features of the penetrating vessel flow discernable from other vessels. The application of the method to the large volume of the OCT scan dataset allows for the automatic mapping and grading of the penetrating arterioles and ascending venules in the scanned area (2.8 mm²) of mouse cortex pre- and post-ischemic strokes *in vivo*.¹² However, despite its successful demonstration, the statistical data analysis procedures (eigen-decomposition and PCA) may increase the complexity of the method. Moreover, the generated penetrating vessel map contains multiple vessel-like artifacts found along the pial branch, which may be challenging to remove prior to grading.

This paper proposes an OCT procedure for the automated detection and quantification of penetrating blood vessels from the OCT raw data of the mouse cerebral cortex. It is hypothesized that penetrating vessels are highlighted with a lower intensity in the mean projection

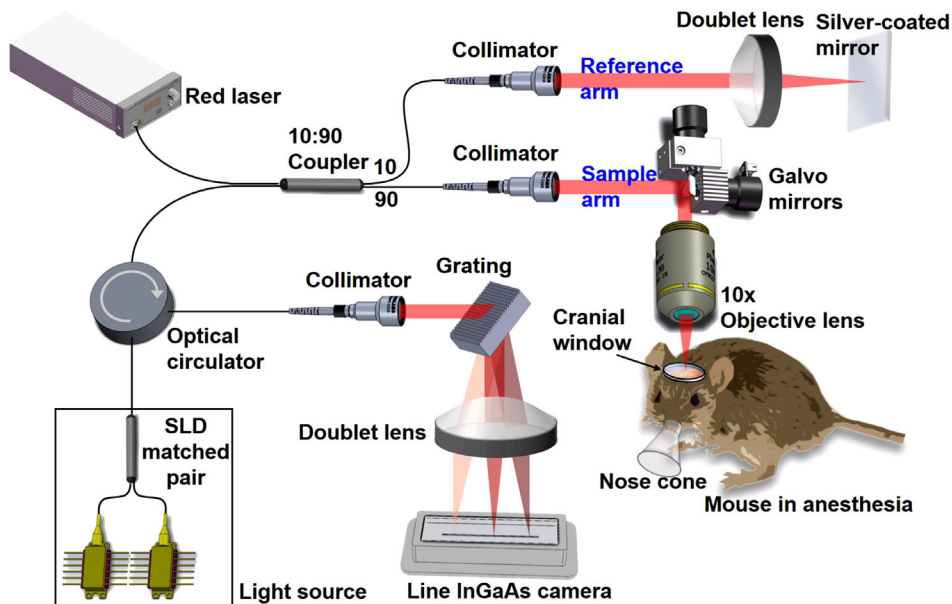


FIGURE 1 Schematic of a custom-built spectral-domain optical coherence tomography (OCT) system. Light from a matched pair of superluminescent diodes (SLDs) was passed through a 90:10 fiber coupler into a mouse cortex via a 10× objective lens and transparent cranial window. Reflected light signals from the mouse cortex interfered with a reference beam and were then detected by a spectrometer consisting of a transmission grating, lens, and one-dimensional (1D) array image sensor.

of the datacube in reflectance and with a higher intensity in the maximum projection of the datacube in flow turbulence. Given these observations, a simple multiplication and thresholding operation is hypothesized to be sufficient to segment the penetrating vessels. Compared with the previous OCT method, the proposed method uses no matrix operations; thus, it has a reduced computational load and requires no additional artifact removal process. The performance of the proposed method was validated using an OCT dataset of a healthy mouse brain, and its applicability was further tested on an ischemic stroke model of mice to examine the ischemia during stroke events.

2 | MATERIALS AND METHODS

2.1 | System setup

We custom-built a spectral-domain OCT system that was similar to those described in previous studies,^{21,22} as shown in Figure 1. In summary, a matched pair of superluminescent diodes (LS2000B, Thorlabs Inc.) was used as a low-coherent light source with an offset emission spectrum for a combined central wavelength of 1340 nm and bandwidth of 110 nm at 3 dB, thus producing an axial (depth) resolution of approximately 7 μm in air. An output beam from the light source was directed to a three-port optical circulator and split at a ratio of 10:90 into a reference arm and a sample arm, respectively, by a 2 × 2 broadband fiber coupler. The interference beam, which was generated by reflections from the

sample and reference arms, exited from the optical circulator and was then detected by a custom-made spectrometer consisting of a transmission grating, achromatic doublet lens, and 1024-pixel InGaAs line scan camera (SUI, Goodrich Corp.) operating at 92 000 axial scans per second (for a free-run mode).

The sample beam was focused onto the surface of the target sample via a 10× objective lens (LSM02, Thorlabs Inc.), thus yielding a lateral resolution of approximately 7 μm . The system sensitivity was measured as ~ 104 dB at a sample illumination power of 4 mW. For OCT imaging, a pair of beam-steering galvanometric mirrors (6200H, Cambridge Technology) were installed to displace the probing beam along the transverse (x) and elevational (y) axes. A 3D OCT dataset was obtained by a raster scanning of the probing beam, which comprised 200 B-scans collected over a cortical surface area of 1.6 mm × 1.6 mm, with each B-scan consisting of 200 A-lines. A 635-nm fiber pig-tailed red laser (S1FC635, Thorlabs Inc.) was coupled to the rest part of the fiber coupler and co-channeled along with the probing beam in the sample arm to help identify the position of the beam spot scanned onto the sample.

2.2 | Animal preparations

This was a prospective study. Eight-week-old male C57BL/6J mice ($n = 3$, weights: 20–25 g) (Charles River Laboratories, Hollister, CA) were selected. The mice were housed at room temperature (22°C) and provided with food and water ad libitum. All the protocols for the

animal experiments were approved by the Institutional Animal Care and Use Committee of the University of Washington, Seattle, USA and were followed in compliance with the US National Research Council's Guide for the Care and Use of Laboratory Animals.

2.3 | Intracranial imaging via cranial window

Surgery was performed on each mouse to seal an optically transparent window into the right parietal bone, as published in previous studies.^{21,23} In summary, the mice were anesthetized by isoflurane inhalation (0.2-L/min O₂ and 0.8-L/min air) using a nose cone prior to surgery, as required to maintain anesthesia during surgery. A heating pad (50-7220F, Harvard Apparatus) was controlled by a rectal thermometer to regulate body temperature from 36.8 to 37°C, and a lubricant ointment was used to moisten eyes as each mouse was placed in a stereotaxic frame. A circular piece of the skull was replaced with a transparent glass coverslip with a diameter of 5 mm, following craniotomy 1-mm posterior and lateral to the bregma. The imaging window was sealed using cyanoacrylate dental cement, thus yielding a flat surface with dimensions of 3 mm × 3 mm through which major pial vessels in the somatosensory cortical region could be imaged using a 10× objective lens.

2.4 | Distal middle cerebral artery occlusion (dMCAO) as an ischemic stroke model

Focal ischemic stroke can be induced in mice via the direct coagulation of the distal middle cerebral artery (MCA).^{23,24} The procedure was in accordance with that presented in Ref. [23] and is summarized as follows. With the anesthetized mouse placed laterally on a surgical table, a 1-cm incision was made between the lateral part of the orbit and the external auditory canal, and skin and temporal muscle were resected and moved aside to expose the skull. After drilling a burr hole on the frontal bone to expose the MCA branch, bipolar cauterizing forceps were used to coagulate the proximal and distal sides of the MCA bifurcation until full occlusion. Within 5–8 min of MCA occlusion, the temporal muscle and skin were restored to their original positions, and the animal was returned to a prone position for OCT imaging.

2.5 | Concept of the method for penetrating vessel counting

The proposed method for penetrating vessel counting was conceptualized with reference to two hypotheses

based on the geometry of cortical penetrating vessels. First, penetrating vessels have weaker OCT intensity signals. Light scattering within turbid media like the brain is typically determined by the sizes of scattering particles and the scattering anisotropic factor (g), which indicates the tendency of light to propagate forward when interacting with a particle.²⁵ With increasing g , the probability for light to be backscattered decreases (i.e., forward scattering becomes more probable than backscattering), making OCT detection more difficult.²⁶ It is common knowledge that an individual red blood cell (RBC) with an average size of $\sim 7\text{-}\mu\text{m}$ scatters near-infrared light at $g = 0.99$, which explains the low likelihood of photons to be backscattered from RBCs within the vessels and detected by OCT.²⁷ For penetrating vessels, especially, forward scattering is dominant throughout the straight and elongated vasculature. Subsequently, penetrating vessels yield low-intensity OCT signals owing to the weak backscattering and additional light absorption by blood, which appears relatively dark in OCT images.

Second, penetrating vessels generate larger disturbances in blood flow at their entries. Physiologic laminar blood flow can transition to turbulent flow at the branching sites in large arteries and veins, and more so at stenotic arterial bifurcations.^{28–31} For penetrating vessels (less than 50- μm diameters⁶) branching off the larger pial network (30–200- μm diameters³²), there is turbulent flow at the branch nodes between the penetrating and pial vessels, which results in randomly fluctuating flow velocities. However, in OCT, the Doppler shift of the light signals backscattered from moving RBCs within a stream of blood is related to the velocity of blood flow. Thus, we can infer that an increase in the blood flow turbulence broadens the spectrum of Doppler shifts, which can be represented as a variance of the power spectrum of OCT signals.³³ For all cerebral vessels in perfusion, the spectral variance would be marginal in laminar flow. However, it increases in accordance with the flow disturbance, which is greater at the entry points of penetrating vessels.

If the abovementioned vascular features (i.e., the weaker backscattering and stronger turbulence) are observed in the penetrating vessels from the OCT measurements, then we can highlight the penetrating vessels from other cerebral vessels in the OCT image, thus allowing for segregation of the penetrating vessels for counting.

2.6 | Protocols for OCT/OCTA and Doppler frequency variance imaging

With the proposed system, OCT/OCTA and Doppler frequency variance measurements were achieved by a single data acquisition process performed using a

scan protocol designed to encompass three imaging formats, that is, the A-, B-, and C-scan. The fast axis (x) scanner cycled through 200 steps for one B-scan. For each step, 50 A-scans were repeated (M-mode scan) at a rate of 20 kHz (time interval of 50 μ s between successive scans), resulting in a total of 10 000 A-scans per B-scan. The acquisition time per B-scan was approximately 625 ms (\sim 1.6 frames/s), including a pullback period for the scanner. For volumetric acquisition, the B-scan process was repeated at 200 different positions in the elevational direction by the slow axis (y) scanner, resulting in a datacube (1024 \times 200 \times 200 pixels) over a cortical surface area (1.6 mm \times 1.6 mm). Approximately 2 min were required to complete data acquisition.

First, the acquired datacubes consisting of complex OCT signals were processed to obtain 200 respective cross-sectional OCT and OCTA images by employing a well-defined OCTA methodology,³⁴ for which each A-line of an OCTA cross section was computed by the eigen-decomposition-based statistical analysis of an ensemble of 50 A-scans of the datacube. This allowed for the decoupling of dynamic scattering components from the raw OCT signal to contrast vessels in perfusion.³⁴ By taking an average of the magnitudes at each depth (z) profile in the 3D OCT dataset, an en face (x - y) map of the cortical structure was reconstructed, and a maximum magnitude projection of each depth (z) profile in the OCTA datacube generated a cortical vessel network map.

Furthermore, the blood flow turbulence was measured with the same datacube used for OCT and OCTA. We calculated the spectral variance σ^2 , which represents the spectral broadening, using the autocorrelation function of the complex OCT signals.³⁵ For the ensemble of time-series complex OCT signals acquired by repeating A-scans at the same location, the following complex multiplication can be conducted:

$$A_1(t) = A(t) \times A^*(t + T) \quad (1)$$

where $A(t)$ is the complex OCT signal at time t , $A^*(t)$ is a complex conjugate, and T is the time interval between the adjacent OCT signals, which is the same as the 1/A-scan rate (1/20 000 s). The autocorrelation R is obtained by integrating $A_1(t')$ for a certain time duration, as follows:

$$R(T, t) = \int_t^{t+nT} A_1(t') dt' \quad (2)$$

where n is the number of consecutive A-scans ($n = 50$); hence, nT is the time elapsed for the M-mode scan. With the autocorrelation function, the spectral variance σ^2 can therefore be calculated using the following equation, as

follows³⁵:

$$\sigma^2 = \frac{1}{T^2} \left\{ 1 - \frac{|R(T)|}{R(0)} \right\} \quad (3)$$

where $R(0)$ is the autocorrelation at $T = 0$, which represents a sum of the ensemble magnitudes. Based on Equation (3), with a decrease in $|R(T)|$ (the lower correlation), the variance increases; the variance is 0 if $|R(T)| = R(0)$, indicating no variation between the OCT signals, which may be measured at the laminar blood flow or the stationary tissues. Thus, the computation generated a datacube of 200 variance cross sections, following collapse into a 2D (x - y) variance map by maximum amplitude projection.

3 | RESULTS

3.1 | Implementation of the penetrating vessel counting method

3.1.1 | Penetrating vessel identification by OCT/OCTA and Doppler frequency variance imaging

Figure 2a presents rendered cortical vasculatures reconstructed from 200 OCTA cross sections on a single mouse brain. Representative vasculature (black box in Figure 2a) can be observed in Figure 2b along with the corresponding OCT cross section (Figure 2c). In both images, Arrows 1 and 2 indicate the positions of an individual pial arteriole and a penetrating arteriole, respectively, where the deep-lying penetrating vessel in the OCTA image can be observed (Figure 2b). It should be noted that the comet tail-like signals below the superficial vessels are artifacts induced by the forward scattering through the vessels.³⁶ However, as shown in Figure 2c, the OCT signal intensities underneath the penetrating arteriole (2) were relatively weaker than those below other vessels, including the arteriole (1), due to lower backscattering along the penetrating vasculature. This can be seen from the depth profiles in Figure 2c, where the means are 3 for (1) and 2.2 for (2) on a logarithmic scale, in accordance with the first hypothesis presented in Section 2.5. By collapsing the 3D OCT data into a 2D projection, followed by averaging, small darker spots indicating the penetrating vessels can be observed in the projection image (Figure 2e). Moreover, Figure 2d, a Doppler frequency variance image at the same location, shows a difference in the variance between the pial arteriole (1) and penetrating arteriole (2) owing to the larger blood flow turbulence at the penetrating arteriole, the magnitudes of which are 28 for (1) and 78 for (2) in frequency variance (MHz), in accordance with the second hypothesis

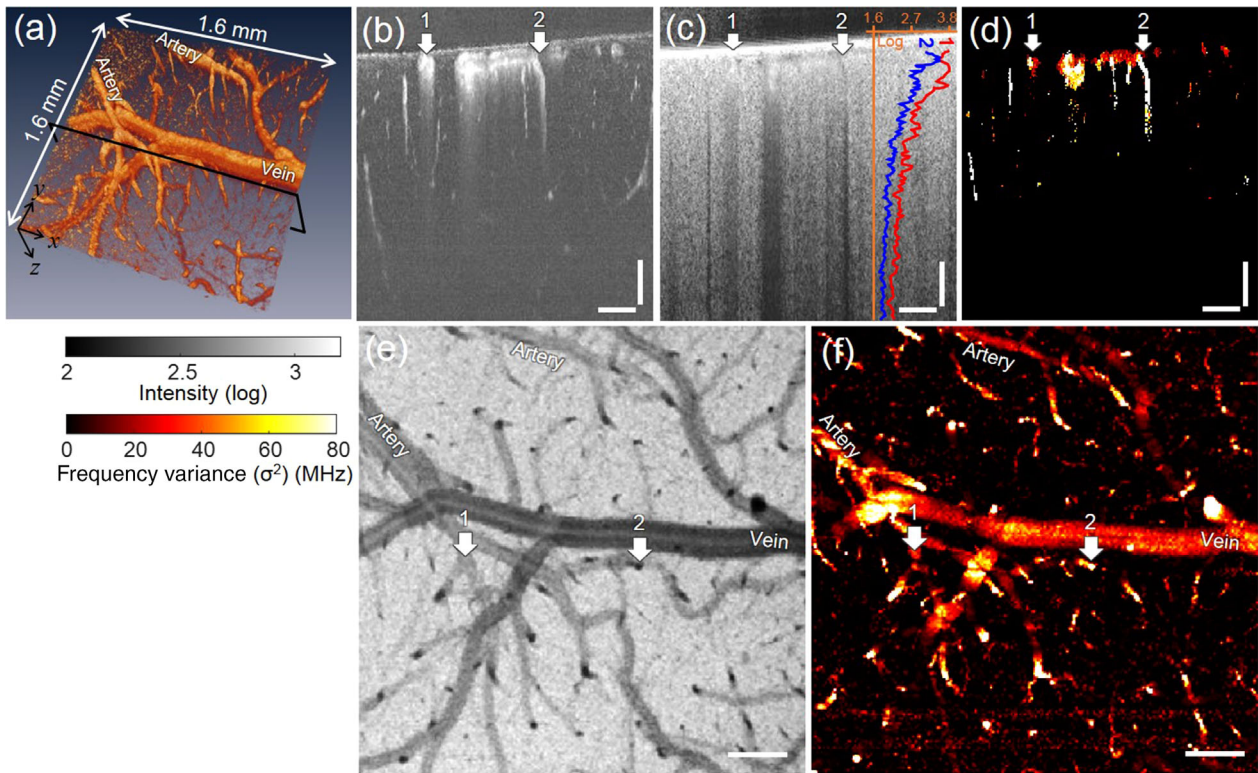


FIGURE 2 Distinctive vascular features observed at the penetrating vessels in the optical coherence tomography (OCT) and Doppler frequency variance images support a simplified analytical method for counting the penetrating vessels: (a) cortical microvasculature reconstructed from the three-dimensional (3D) OCT angiography (OCTA) dataset of a healthy young mouse; (b) cross-sectional (x - z) OCTA image captured from the black box in (a), which exhibits functional cortical vessels involving a pial arteriole (1) and penetrating arteriole (2); (c) corresponding cross-sectional OCT image where the shadow cast by the blood flow is darker at the penetrating arteriole (2) than the pial arteriole (1), as can be observed from the comparison of the depth profiles along (1) and (2); (d) corresponding Doppler frequency variance image representing the severity of turbulence in the blood flow. The variance at the penetrating arteriole (1) is greater than that at the pial arteriole (2); (e) mean projection of the 3D OCT data, and (f) maximal projection of the 3D Doppler frequency variance data. The penetrating vessels are presented as darker and brighter spots in (e) and (f), respectively (scale bars: $200\ \mu\text{m}$).

in the Section 2.5. A maximum projection (Figure 2f) of the 3D variance data exhibited brighter spots ($>60\ \text{MHz}$), indicating the penetrating vessels.

3.1.2 | Penetrating vessel segmentation and quantification

As distinguishing features of the penetrating vessels were observed in the two different imaging modalities, these features were employed to accurately and automatically segment the penetrating vessels. To quantify the vessel population, we overemphasize the penetrating vessels in the image through the procedure in Figure 3, which facilitates the localization of the vessels. Moreover, this strategy can be realized by combining the mean projection image from the 3D OCT data (Figure 2e) and the maximum projection image from the 3D Doppler frequency variance data (Figure 2f). Figure 3 illustrates all the procedures employed to count the penetrating vessels. In particular, the mean projection (Figure 3a, the same as Figure 2e) was

normalized and inverted, and then renormalized to Figure 3c, in which the penetrating vessels had maximal values. This normalized image was multiplied with the normalized maximal projection image (Figure 3b, the same as Figure 2e). This multiplication resulted in amplification of the vessel contrast over the other surface vessels, as shown in Figure 3d. The threshold value was set to 0.65 empirically based on a histogram of Figure 3d obtained from the healthy young mice (Figure 3e). Moreover, based on this threshold, the resulting projection was turned into a binary mask (Figure 3f), which only indicated the penetrating vessels. Based on the overlapping of Figure 3f with (a), the segmented spots (green) in Figure 3a were accurately matched with the locations of the penetrating vessels in the overlaid image (Figure 3f), which was confirmed by identifying the elongated vasculatures in the OCTA cross sections corresponding to the individual spots in the colored boxes (Figure 3h). A simple region-counting algorithm applied to the binary image counted the spots, yielding the total number of vessels ($n = 63$) in the image, as shown in Figure 3i. All image analyses were performed

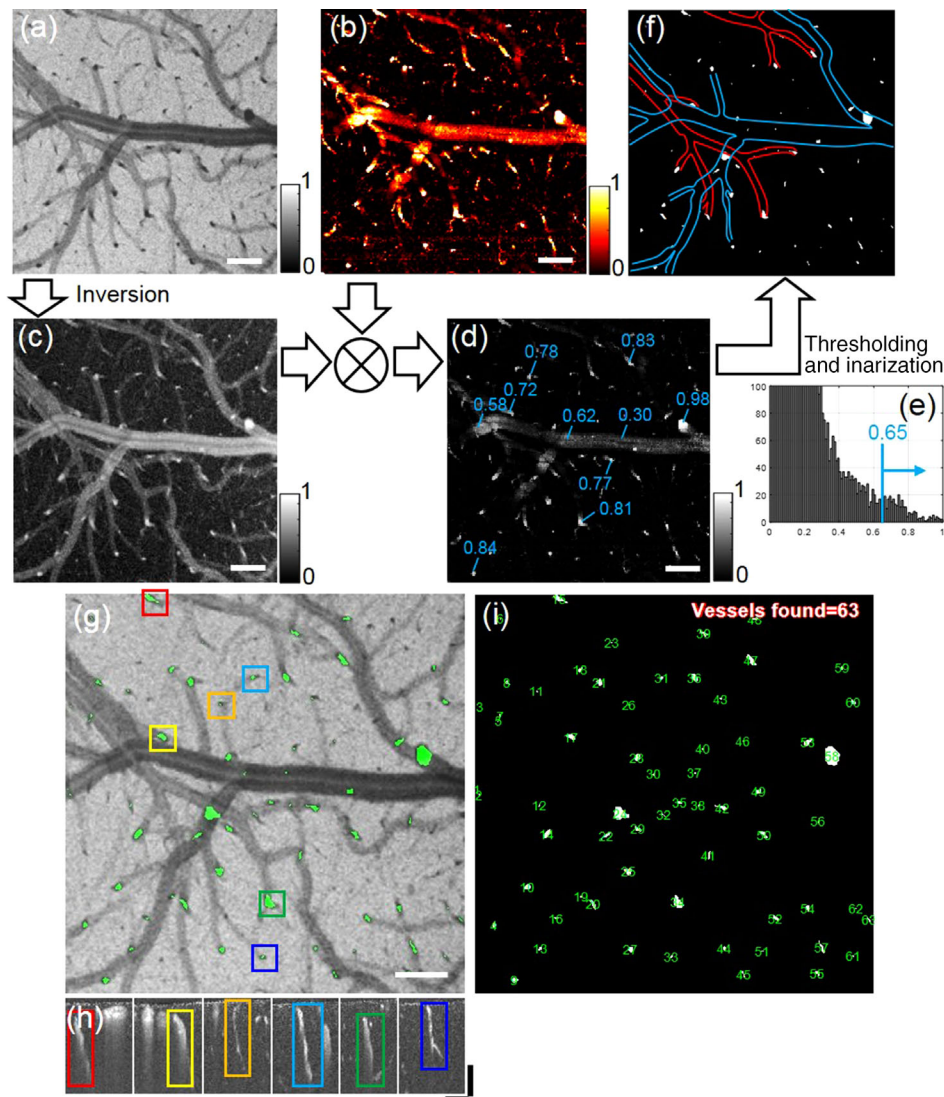


FIGURE 3 Illustration of all the procedures for the counting of penetrating vessels, with the representative images in Figure 2: (a) normalized mean projection of the three-dimensional (3D) optical coherence tomography (OCT) data and (b) normalized maximal projection of the Doppler frequency variance data were combined by inverting the OCT projection with a maximum and normalizing (c) and multiplying (c) elementwise with (b) to highlight the penetrating vessels; (e) a threshold for filtering out the penetrating vessels was determined empirically from a variance histogram; (f) binarized result of (d) with threshold extracts penetrating vessels (white) matched to locations (end points or en passant) of the pial arterioles (hand-segmented, blue) and the pial venules (hand-segmented, red); (g) segmented spots (green) correspond to the penetrating vessels in the OCT projection (a), as confirmed by (h) the cross section of the vessels matched between images by colored bounding boxes; (i) finally, the segmented vessels were identified and quantified (total counts = 63). Scale bars: 200 μm (white bars), 50 μm (black bars)

on a custom-built program written in MATLAB. However, to estimate the accuracy of the proposed method, one examiner with expertise on OCT was asked to grade the penetrating vessels under guidelines instructing the examiner to manually count the dark spots on the mean projection OCT image (Figure 3a). The total count was 69. Assuming that the count was the actual number of penetrating vessels (reference), the accuracy could be calculated as the ratio of the measured count to the reference and was found to be 89.95%. This was further estimated as 87.11% for all the mice ($n = 3$).

3.2 | Application of method to ischemic stroke model of mice

We demonstrated the feasibility of the proposed method for assessing the population of functional penetrating vessels subject to the alteration in blood perfusion during ischemic strokes. The distal MCA occlusion (dMCAO) mouse model^{23,24} was used to induce focal ischemia in the cerebral cortex. Figure 4 presents the experimental results before (baseline) and 30 min after the onset of focal ischemic stroke in

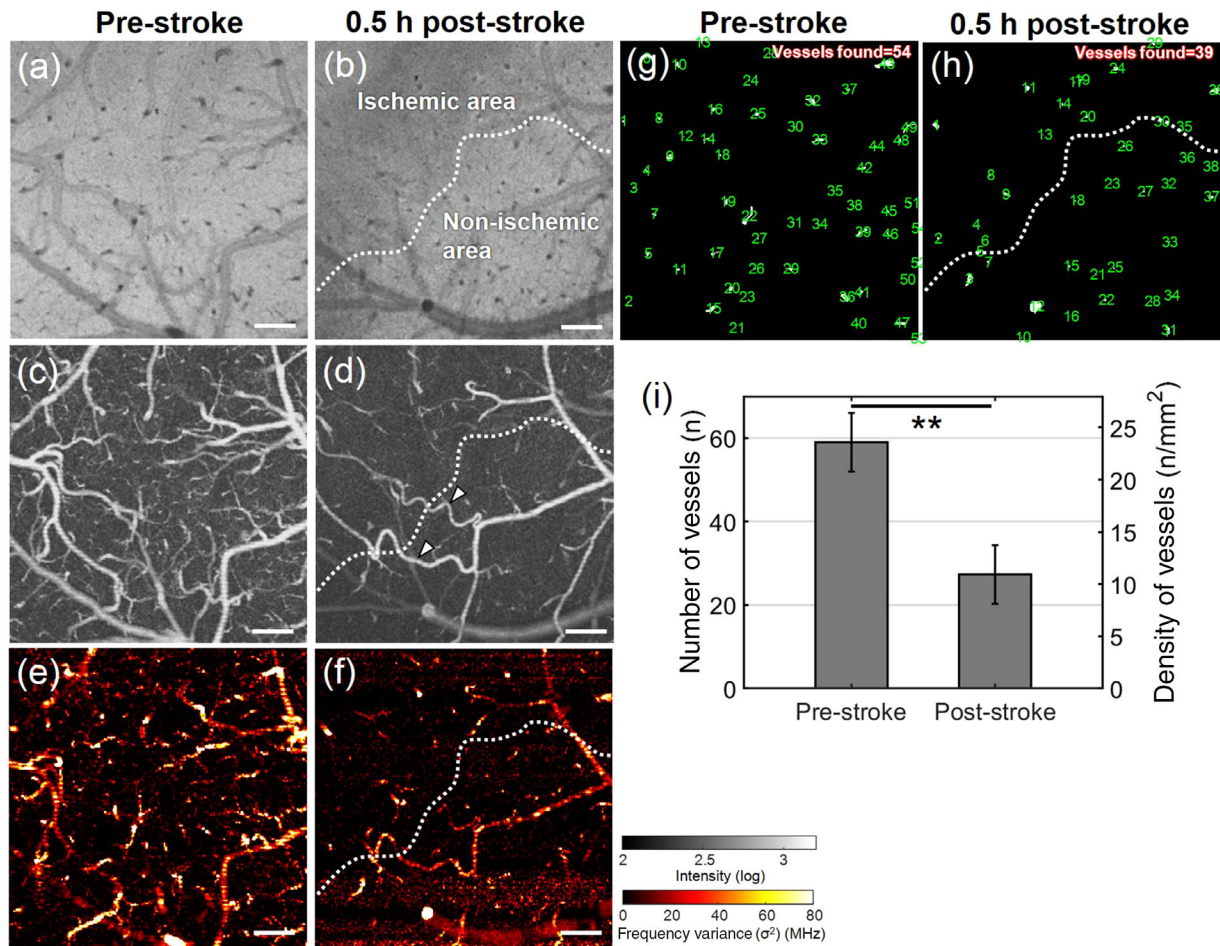


FIGURE 4 Comparison of the quantified penetrating vessels by in vivo imaging of a mouse cerebral cortex pre- and post-stroke. The focal ischemia was induced by the permanent coagulation of a distal middle cerebral artery (dMCA) using electrocoagulation in mice ($n = 3$), producing a rarefaction of blood circulation and subsequent cortical infarction around the ischemic lesion: (a, c, e) projection images of the cortical structure, blood perfusion, and Doppler frequency variance pre-stroke. A total of 54 penetrating vessels were counted in the imaging region (g) during normal perfusion, which corresponds to 21.09 vessels/mm²; (b, d, f) projection images of the cortical structure, blood perfusion, and Doppler frequency variance 30 min after stroke. Changes in the scattering (b), perfusion (d), and flow turbulence (f) were observed with a reduction in the number of normally perfused penetrating vessels to 39 (h), which correspond to 15.23 vessels/mm²; (i) quantification of the number of total penetrating vessels in perfusion pre- and post-stroke (** $p < 0.005$ [paired t test]). Data are presented as mean \pm SEM ($n = 3$ mice; one region imaged per mouse). Scale bars: 200 μ m.

the same mouse cortex, where important qualitative and quantitative changes can be observed. In particular, in comparison with the cortical region pre-stroke, the ischemic area post-stroke exhibited lower contrast in OCTA (see Figure 4c,d) and in Doppler frequency variance projections (see Figure 4e,f) of both penetrating and surface pial vessels, thus indicating reduced blood flow at the ischemic region and the supply of blood via anastomoses by activated collateral vessels (arrowheads in Figure 4d) from the nonischemic region. However, in the OCT projections, the dark contrasts at the penetrating vessels were either lighter than those in the pre-stroke data or not observable (see Figure 4a,b). This may be due to the weakened forward scattering and light absorption due to the failure of blood flow, in addition to the probable deflection of the penetrating vasculature.²¹ Accordingly, the contrast-degraded

penetrating vessels in the OCT and Doppler frequency variance projections could exhibit variance values below the threshold. These values were considered abnormal in perfusion and excluded prior to counting. Thereafter, the penetrating vessels were quantified: 54 penetrating vessels were counted in the normal perfusion on pre-stroke (Figure 4g), which corresponded to a vessel density of 21.09 vessels/mm². Following dMCAO, 39 functional penetrating vessels were counted (Figure 4f), or 15.23 vessels/mm². Although both ischemic and nonischemic regions appeared in Figure 4f, the drop in vessel count and density was observed in the ischemic region. For all the mice ($n = 3$), the vessel counts (mean \pm SEM) pre/post-stroke were 59 ± 7 and 27.3 ± 7 , respectively, when statistically quantified in Figure 4i. Therefore, with the mean values, the densities of the penetrating vessels were calculated

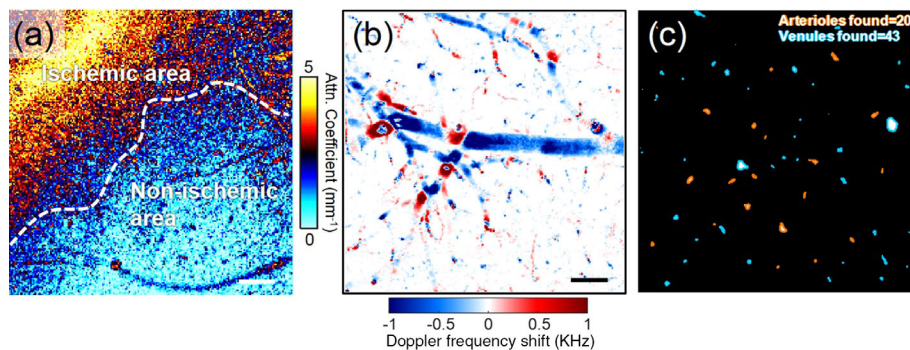


FIGURE 5 (a) Attenuation projection image of the cortical region (Figure 4b) of the mouse postischemic stroke, which represents the extent of light absorption and scattering through the cortical tissue with respect to depth. The dotted line demarcates the ischemic territory (highly attenuated) and the nonischemic area (weakly attenuated), which was indicated in Figure 4b,d,f,h. (b) Mean Doppler frequency shift of the projection image obtained from the same area as the cortical region of the healthy young mouse in Figure 3a, thus exhibiting the bidirectionality of blood flow—induced polarity with respect to magnitude. The positive values (reddish) resulted from the upstream of blood, and the negative values (bluish) resulted from the downstream of blood. (c) The multiplication of (b) and binary image of penetrating vessel spots (Figure 3f) allowed for the sorting of the descending arterioles (orange) and ascending venules (light blue) from the all the penetrating vessels, which could be counted separately (scale bars: 200 μm).

as 23.05/mm² (pre-stroke) and 10.66/mm² (post-stroke), indicating a significant decrease of more than 45% after stroke. The vessel densities were similar to the results reported in previous studies.^{6,7,12}

4 | DISCUSSION

This paper proposes a method that can accurately locate and quantify penetrating vessels in cerebral cortex OCT images. Moreover, changes in the population of the vessels in the ischemic stroke model of mice were demonstrated using the proposed method. Compared with conventional vessel counting approaches based on fluorescence imaging or DOCT, the approach can count and grade the penetrating vessels in an automated manner.

In particular, the algorithmic complexity of the proposed method was lower than that of previous algorithms for the detection of penetrating vessels in OCT. Wei et al. proposed an OCT data-based method for eigen-decomposition analysis followed by PCA. The computational complexity of eigenvalue decomposition is the same as that of matrix ($n \times n$) multiplication $O(n^3)$, where all simple arithmetical computations are assumed to have an identical cost.¹² In practice, this implies that the eigenvalue decomposition of an OCT dataset with dimensions of 400×400 would require eight times as many computational operations as a 200×200 dataset, despite only a factor of four increase in the measurement time. In contrast, the proposed method only performs elementwise operations on the projections of A-lines, which scales as the number of A-lines captured: $O(n^2)$ in the dimension of the OCT field. In addition, the blob counting (Figure 3i) can be more rapid than the eigenvalue decomposition and PCA process and is easily scalable.

However, limitations of this study include difficulty in using the proposed method for the human cerebral cortex with the present OCT device owing to its limited scan range ($1.6 \times 1.6 \text{ mm}^2$). In addition, human cortical sites are inaccessible to the stand-alone probe after exposure of the brain cortex by craniotomy. Hartmann et al. recently reported the first visualization of the human brain cortex in vivo using wide-field OCT connected to the port of a surgical microscope.³⁷ The proposed method has the advantages of the intraoperative OCT technology developed for neuroimaging in operation, allowing for the penetrating blood vessels of stroke patients to be counted.

There was a minor mismatch between the baseline and post-stroke scans of each mouse cortex (Figure 4). This was due to difficulty faced in returning the mouse to its baseline position after dMACO surgery. In future research, mismatches will be mitigated by co-registering the projection images using established medical image registration techniques.^{38,39}

The dotted line in Figure 4b,d,f,h indicates a boundary between ischemic and nonischemic territories, as extracted from an attenuation image (Figure 5a) obtained by applying a tissue attenuation mapping technique to the OCT datacube post-stroke.⁴⁰ Contrast in this image (Figure 5a) represents the magnitudes of the attenuation coefficients ($\#/mm$), which describe the extent of absorption and scattering of OCT signal intensities through the cortical tissue. The correlation of the ischemic area to strong local attenuation (yellowish signal band in Figure 5a) as well as use of the attenuation zone (i.e., the dotted line in Figure 5a) as the border of ischemic area was confirmed in a previous mouse cortex OCT study.²¹

We obtained Doppler frequency variance images using the autocorrelation function of the complex OCT signals, as expressed by Equation (3). However, the

autocorrelation technique can provide additional information on the mean angular frequency ($\bar{\omega}$), a centroid of Doppler frequency shifts, and it may be used to segregate the penetrating arterioles and ascending venules in grading.³⁵ For example, the mean angular frequency can be expressed as $\bar{\omega} = \phi(T)/T$, where $\phi(T)$ denotes the phase gain obtained from $R(T, t)$:

$$\phi(T, t) = \tan^{-1} \frac{\text{Im}(R(T, t))}{\text{Re}(R(T, t))} \quad (4)$$

where $\text{Re}(R(T, t))$ and $\text{Im}(R(T, t))$ are real and imaginary components of $R(T, t)$, respectively. Given that the phase gain $\phi(T)$ is a signed value, and the polarity is related to the direction of the blood flow vector against the OCT probing beam, the sign of $\bar{\omega}$ indicates flow direction. Figure 5b presents an example of the mean angular frequency map obtained from the OCT datacube in Figure 3a, where negative values (blue) correspond to upward blood flow and positive values (red) correspond to downward blood flow. By multiplying Figure 5b with Figure 3f, we can obtain a simple product that nominally allows for the respective counting of penetrating arterioles and ascending venules, as shown in Figure 5c, following the resolution of 2-pi phase ambiguities between adjacent A-scans.⁴¹

5 | CONCLUSION

In conclusion, a new OCT image analysis method for quantifying the perfusing penetrating blood vessels in the OCT of the mammalian cortex in vivo is outlined and was demonstrated on a small animal model of stroke. It was verified that reduced OCT contrast and increased Doppler contrast in penetrating vessels can be combined algorithmically to obtain a segmentation of the penetrating vessels. An accuracy of more than 87% was achieved with the proposed method in the grading of the penetrating vessels in perfusion. In the stroke experiment, the counting results obtained with the proposed approach revealed a significant decrease in the perfused penetrating vessels in the ischemic territory, resulting in a reduction of more than 45% in the vessel density even 30 min after stroke. The proposed method can be performed with data from standard OCT setups and can reduce the algorithmic complexity of the automated grading of penetrating vessels. Thus, it can be applied in small animal models of ischemic stroke and neurological diseases.

ACKNOWLEDGMENTS

This work was supported by the Basic Science Research Program [Grant nos. 2020R1F1A107403311, 2020R1F1A1072912, 2019R1A2C2084122], Engineering Research Center (ERC) [Grant no.

2020R1A5A1018052], and Medical Research Center (MRC) [Grant no. 2018R1A5A2020732] through the National Research Foundation of Korea (NRF) funded by the Ministry of Science and ICT; the Korean Ministry of Trade, Industry and Energy under the Industrial Technology Innovation Program [Grant no. 20000843]; and the Ministry of Health and Welfare, the Korea Health Industry Development Institute (KHIDI) [Grant no. HI18C2391].

CONFLICT OF INTEREST

The authors declare that there is no conflict of interest that could be perceived as prejudicing the impartiality of the research reported.

REFERENCES

1. Nishimura N, Schaffer CB, Friedman B, Lyden PD, Kleinfeld D. Penetrating arterioles are a bottleneck in the perfusion of neocortex. *Proc Natl Acad Sci USA*. 2007;104(1):365-370. <https://doi.org/10.1073/pnas.0609551104>
2. Schaffer CB, Friedman B, Nishimura N, et al. Two-photon imaging of cortical surface microvessels reveals a robust redistribution in blood flow after vascular occlusion. *PLoS Biol*. 2006;4(2):e22. <https://doi.org/10.1371/journal.pbio.0040022>
3. Baran U, Li Y, Wang RK. Vasodynamics of pial and penetrating arterioles in relation to arteriolo-arteriolar anastomosis after focal stroke. *Neurophotonics*. 2015;2(2):025006. <https://doi.org/10.1117/1.NPh.2.2.025006>
4. Blinder P, Tsai PS, Kaufhold JP, Knutsen PM, Suhl H, Kleinfeld D. The cortical angiome: an interconnected vascular network with noncolumnar patterns of blood flow. *Nat Neurosci*. 2013;16(7):889-897. <https://doi.org/10.1038/nn.3426>
5. Blinder P, Shih AY, Rafie C, Kleinfeld D. Topological basis for the robust distribution of blood to rodent neocortex. *Proc Natl Acad Sci USA*. 2010;107(28):12670-12675. <https://doi.org/10.1073/pnas.1007239107>
6. Shih AY, Blinder P, Tsai PS, et al. The smallest stroke: occlusion of one penetrating vessel leads to infarction and a cognitive deficit. *Nat Neurosci*. 2013;16(1):55-63. <https://doi.org/10.1038/nn.3278>
7. Nguyen J, Nishimura N, Fetcho RN, Iadecola C, Schaffer CB. Occlusion of cortical ascending venules causes blood flow decreases, reversals in flow direction, and vessel dilation in upstream capillaries. *J Cereb Blood Flow Metab*. 2011;31(11):2243-2254. <https://doi.org/10.1038/jcbfm.2011.95>
8. Joo IL, Lai AY, Bazzigaluppi P, et al. Early neurovascular dysfunction in a transgenic rat model of Alzheimer's disease. *Sci Rep*. 2017;7(1):46427. <https://doi.org/10.1038/srep46427>
9. Suter OC, Sunthorn T, Kraftsik R, et al. Cerebral hypoperfusion generates cortical watershed microinfarcts in Alzheimer disease. *Stroke*. 2002;33(8):1986-1992. <https://doi.org/10.1161/01.STR.0000024523.82311.77>
10. Coelho-Santos V, Berthiaume AA, Ornelas S, Stuhlmann H, Shih AY. Imaging the construction of capillary networks in the neonatal mouse brain. *Proc Natl Acad Sci USA*. 2021;118(26):e2100866118. <https://doi.org/10.1073/pnas.2100866118>
11. Li Y, Choi WJ, Wei W, et al. Aging-associated changes in cerebral vasculature and blood flow as determined by quantitative optical coherence tomography angiography. *Neurobiol Aging*. 2018;70:148-159. <https://doi.org/10.1016/j.neurobiolaging.2018.06.017>
12. Wei W, Li Y, Deegan AJ, Wang RK. Mapping and quantitating penetrating vessels in cortical brain using eigen-decomposition of OCT signals and subsequent principal component analysis.

- IEEE J Sel Top Quantum Electron.* 2019;25(1):1-9. <https://doi.org/10.1109/JSTQE.2018.2863573>
13. Fujimoto JG, Pitris C, Boppart SA, Brezinski ME. Optical coherence tomography: an emerging technology for biomedical imaging and optical biopsy. *Neoplasia.* 2000;2(1-2):9-25. <https://doi.org/10.1038/sj.neo.7900071>
 14. Yaqoob Z, Wu J, Yang C. Spectral domain optical coherence tomography: a better OCT imaging strategy. *BioTech.* 2005;39(6S):S6-S13. <https://doi.org/10.2144/000112090>
 15. Chen CL, Wang RK. Optical coherence tomography based angiography [Invited]. *Biomed Opt Express.* 2017;8(2):1056. <https://doi.org/10.1364/BOE.8.001056>
 16. Li Y, Chen J, Chen Z. Advances in Doppler optical coherence tomography and angiography. *Transl Biophotonics.* 2019;1(1-2):e201900005. <https://doi.org/10.1002/tbio.201900005>
 17. Mariampillai A, Standish BA, Moriyama EH, et al. Speckle variance detection of microvasculature using swept-source optical coherence tomography. *Opt Lett.* 2008;33(13):1530. <https://doi.org/10.1364/OL.33.001530>
 18. Fingler J, Schwartz D, Yang C, Fraser SE. Mobility and transverse flow visualization using phase variance contrast with spectral domain optical coherence tomography. *Opt Express.* 2007;15(20):12636. <https://doi.org/10.1364/OE.15.012636>
 19. An L, Qin J, Wang RK. Ultrahigh sensitive optical microangiography for *in vivo* imaging of microcirculations within human skin tissue beds. *Opt Express.* 2010;18(8):8220. <https://doi.org/10.1364/OE.18.008220>
 20. Shi L, Qin J, Reif R, Wang RK. Wide velocity range Doppler optical microangiography using optimized step-scanning protocol with phase variance mask. *J Biomed Opt.* 2013;18(10):106015. <https://doi.org/10.1117/1.JBO.18.10.106015>
 21. Choi WJ, Li Y, Wang RK. Monitoring acute stroke progression: multi-parametric OCT imaging of cortical perfusion, flow, and tissue scattering in a mouse model of permanent focal ischemia. *IEEE Trans Med Imaging.* 2019;38(6):1427-1437. <https://doi.org/10.1109/TMI.2019.2895779>
 22. Li Y, Rakymzhan A, Tang P, Wang RK. Procedure and protocols for optical imaging of cerebral blood flow and hemodynamics in awake mice. *Biomed Opt Express.* 2020;11(6):3288. <https://doi.org/10.1364/BOE.394649>
 23. Li Y, Baran U, Wang RK. Application of thinned-skull cranial window to mouse cerebral blood flow imaging using optical microangiography. Ng LG, ed. *PLoS One.* 2014;9(11):e113658. <https://doi.org/10.1371/journal.pone.0113658>
 24. Llovera G, Roth S, Plesnila N, Veltkamp R, Liesz A. Modeling stroke in mice: permanent coagulation of the distal middle cerebral artery. *J Visual Exp.* 2014;89(89):51729. <https://doi.org/10.3791/51729>
 25. Kienle A, Wetzel C, Bassi A, Comelli D, Taroni P, Pifferi A. Determination of the optical properties of anisotropic biological media using an isotropic diffusion model. *J Biomed Opt.* 2007;12(1):014026. <https://doi.org/10.1117/1.2709864>
 26. Kodach VM, Faber DJ, van Marle J, van Leeuwen TG, Kalkman J. Determination of the scattering anisotropy with optical coherence tomography. *Opt Express.* 2011;19(7):6131. <https://doi.org/10.1364/OE.19.006131>
 27. Friebe M, Roggan A, Müller G, Meinke M. Determination of optical properties of human blood in the spectral range 250 to 1100 nm using Monte Carlo simulations with hematocrit-dependent effective scattering phase functions. *J Biomed Opt.* 2006;11(3):034021. <https://doi.org/10.1117/1.2203659>
 28. Stehbens WE. Turbulence of blood flow. *Exp Physiol.* 1959;44(1):110-117. <https://doi.org/10.1113/expphysiol.1959.sp001365>
 29. Sidik WA, Mazumdar JN. A mathematical study of turbulent blood flow through an arterial bifurcation. *Australas Phys Eng Sci Med.* 1994;17(1):1-13.
 30. Lee SE, Lee SW, Fischer PF, Bassiouny HS, Loth F. Direct numerical simulation of transitional flow in a stenosed carotid bifurcation. *J Biomech.* 2008;41(11):2551-2561. <https://doi.org/10.1016/j.jbiomech.2008.03.038>
 31. Banks J, Bressloff NW. Turbulence modeling in three-dimensional stenosed arterial bifurcations. *J Biomech Eng.* 2007;129(1):40-50. <https://doi.org/10.1115/1.2401182>
 32. Gao YR, Drew PJ. Effects of voluntary locomotion and calcitonin gene-related peptide on the dynamics of single dural vessels in awake mice. *J Neurosci.* 2016;36(8):2503-2516. <https://doi.org/10.1523/JNEUROSCI.3665-15.2016>
 33. Wang RK, Zhang Q, Li Y, Song S. Optical coherence tomography angiography-based capillary velocimetry. *J Biomed Opt.* 2017;22(6):066008. <https://doi.org/10.1117/1.JBO.22.6.066008>
 34. Yousefi S, Zhi Z, Wang RK. Eigendecomposition-based clutter filtering technique for optical microangiography. *IEEE Trans Biomed Eng.* 2011;58(8):2316-2323. <https://doi.org/10.1109/TBME.2011.2152839>
 35. Kasai C, Namekawa K, Koyano A, Omoto R. Real-time two-dimensional blood flow imaging using an autocorrelation technique. *IEEE Trans Ultrason.* 1985;32(3):458-464. <https://doi.org/10.1109/T-SU.1985.31615>
 36. Choi WJ, Paulson B, Yu S, Wang RK, Kim JK. Mean-subtraction method for de-shadowing of tail artifacts in cerebral OCTA images: a proof of concept. *Materials.* 2020;13(9):2024. <https://doi.org/10.3390/ma13092024>
 37. Hartmann K, Stein KP, Neyazi B, Sandalcioğlu IE. First *in vivo* visualization of the human subarachnoid space and brain cortex via optical coherence tomography. *Ther Adv Neurol Disord.* 2019;12:175628641984304. <https://doi.org/10.1177/1756286419843040>
 38. Wei DW, Deegan AJ, Wang RK. Automatic motion correction for *in vivo* human skin optical coherence tomography angiography through combined rigid and nonrigid registration. *J Biomed Opt.* 2017;22(6):066013. <https://doi.org/10.1117/1.JBO.22.6.066013>
 39. Chu Z, Zhou H, Cheng Y, Zhang Q, Wang RK. Improving visualization and quantitative assessment of choriocapillaris with swept source OCTA through registration and averaging applicable to clinical systems. *Sci Rep.* 2018;8(1):16826. <https://doi.org/10.1038/s41598-018-34826-5>
 40. Vermeer KA, Mo J, Weda JJA, Lemij HG, de Boer JF. Depth-resolved model-based reconstruction of attenuation coefficients in optical coherence tomography. *Biomed Opt Express.* 2014;5(1):322. <https://doi.org/10.1364/BOE.5.000322>
 41. Xia S, Huang Y, Peng S, Wu Y, Tan X. Robust phase unwrapping for phase images in Fourier domain Doppler optical coherence tomography. *J Biomed Opt.* 2017;22(3):036014. <https://doi.org/10.1117/1.JBO.22.3.036014>

How to cite this article: Choi WJ, Li Y, Wang RK, Kim JK. Automated counting of cerebral penetrating vessels using optical coherence tomography images of a mouse brain *in vivo*. *Med. Phys.* 2022;1–11. <https://doi.org/10.1002/mp.15775>